



Study of microstructure evolution in the aluminum–magnesium alloy AlMg6 after explosive welding and heat treatment

Andrey Malakhov¹ · Ivan Saikov¹ · Igor Denisov¹ · Alexander Berdychenko² · Sergey Ivanov² · Nemat Niyozbekov¹ · Sergey Mironov³ · Rustam Kaibyshev³ · Pavel Dolzhenko³

Received: 27 May 2024 / Accepted: 4 September 2024 / Published online: 11 September 2024
© The Author(s), under exclusive licence to Springer-Verlag London Ltd., part of Springer Nature 2024

Abstract

Aluminum–magnesium alloys are widely used in the shipbuilding and railcar industries because of their high specific strength and corrosion resistance. However, the welding of aluminum–magnesium alloys to steel poses a number of significant issues, mainly due to the formation of brittle intermetallic compounds (IMCs) and adiabatic shear bands (ASBs). The effects of IMCs on the mechanical properties of joints have been well researched, but there is a limited understanding of how ASBs and magnesium affect these properties. In this work, the effects of ASBs and Mg_2Al_3 on the mechanical properties of explosive-welded bimetallics are studied. Optical microscopy, electron microscopy, confocal laser scanning microscopy, and electron backscatter diffraction (EBSD) were performed. Additionally, Vickers hardness tests, tear strength tests, and bending tests were carried out to determine the mechanical properties of the specimens. The results of the study revealed that at the weld interface after explosive welding, a zone of fine dark-etching Mg_2Al_3 phase accumulation up to 10 μm thick and an ASB zone up to 400 μm thick formed. The thickness and included volume of both zones increase from 3 to 20 vol.% with increasing detonation velocity. The tear strength also increases (from 80 to 230 MPa). After heat treatment at 200 °C for 1 h, the specimens survived at twice the bending angle, indicating good plastic properties. Thus, the results help elucidate the influence of Mg_2Al_3 and ASBs on the properties of bimetallics with AlMg6 alloys obtained via explosive welding.

Keywords Al–Mg alloys · Explosive welding · EBSD analysis · Weld interface · Microstructure

1 Introduction

Aluminum–magnesium alloy (AlMg) is the most commonly used material for various applications, such as the aerospace, shipbuilding, and automotive and railcar industries, because of its light weight, suitable mechanical properties and corrosion resistance, as well as good weldability and machinability [1–3]. For example, owing to its good corrosion resistance in seawater environments and high tensile strength (up to 420 MPa), AlMg is widely used as a material for high-pressure vessels, ships, and other marine

structures. The high tensile strength is due to the presence of Mg in the AlMg. The higher the Mg content is, the greater the tensile strength of the AlMg alloy. However, when this content increases to 7% or more, the corrosion resistance of the AlMg decreases. Therefore, the appropriate Mg content for the combination of strength and corrosion properties is approximately 6% (i.e., AlMg6).

However, it is not always advisable to make marine structures entirely of AlMg because of its low stiffness and low melting points compared with those of steel or titanium. Therefore, the elements of a construction that undergo significant mechanical stresses are often made of steel or other alloys. For example, in the shipbuilding industry, ship hulls are made of steel, whereas chimney casings, wheelhouses, and deck bridges are made of AlMg. This reduces the overall ship weight up to 50–60%, thus increasing the deadweight tonnage and improving the overall ship performance.

Various fusion welding methods are used to join parts made of AlMg and steel [4]. During the fusion welding process, metal temperatures can reach 1800 °C [5]. The authors

✉ Nemat Niyozbekov
nemat199595@mail.ru

¹ Merzhanov Institute of Structural Macrokinetics and Materials Science, Russian Academy of Sciences, Chernogolovka, Moscow Region 142432, Russia

² Polzunov Altai State Technical University, Barnaul 656038, Russia

³ Belgorod State University, Belgorod 308015, Russia

of [6] reported that the metal temperature reaches 3623 K. When dissimilar materials are welded, such high temperatures contribute to the formation of intermetallic compounds (IMCs), which reduce the mechanical properties of the material [7]. Therefore, pressure welding methods are mainly used because the joint is formed in the solid phase. At present, the joints between AlMg and steel are obtained via the following pressure welding methods: friction welding [8], diffusion welding [9], ultrasonic welding [10], cold rolling [11], magnetic pulse welding [12], hot isostatic pressing [13], and explosive welding (EW) [14–16].

EW is the most suitable method for obtaining a joint of AlMg with steel due to its high process velocity and high pressure, resulting in significant deformation and local heating of the welded surfaces. The authors of [17] reported that the local temperature at the weld interface reaches 10^4 – 10^5 K, which exceeds the melting point of any metal. In [18], the authors measured the temperature of the shock-compressed gas (SCG) region in a welding gap using optical pyrometry and showed that this temperature reached 4100–4400 K. This temperature value depends on the detonation velocity: the higher the detonation velocity is, the higher the temperature. In [19], they investigated the weld interface of AZ31B–Al5052 obtained by explosive welding. An $\text{Al}_{12}\text{Mg}_{17}$ IMC formed due to local melting of the welded surfaces. In addition, the residual stress that forms in materials due to different coefficients of linear expansion affects the quality of the welded joint. For example, in [20], the residual stress in an Al–Cu–Al multilayer composite material obtained by explosive welding was investigated. The authors showed that the residual stress on the surface is particularly undesirable since it increases susceptibility to fatigue and stress corrosion.

Additionally, adiabatic shear bands (ASBs) are formed within the AlMg alloy, which causes inhomogeneity in the material structure and can also lead to material failure. ASBs are narrow zones of intense shearing strain

that develop during severe deformation of ductile materials [21]. They appear to be due to the effect of the localization of plastic deformation in the process of material loading. The localization of plastic deformation in metals and alloys under dynamic loading is a process that depends on the rate and magnitude of deformation, temperature, and evolution of the material structure.

In [22], optical and electron microscopy revealed the presence of many ASBs in an AlMg6–AlMg6 bimetal after EW. The number of ASBs is roughly the same in both layers. The present work is an extension of previous work [22]. Here, a more detailed study of the microstructure of ASBs and the weld interface was carried out using EBSD analysis and confocal laser scanning microscopy. The evolution of the microstructure of the AlMg6–AlMg6 weld interface after heat treatment was also investigated, and additional mechanical tests were performed on the bimetallic specimens.

2 Materials and methods

2.1 Initial materials and EW parameters

Figure 1 shows the microstructure of the initial AlMg6 plate. The grains of the α -solid solution (α -phase) are elongated along the rolling direction. Small (Fe, Mn)Al₆ inclusions and the β -phase (Mg_2Al_3) are present along the grain boundaries [23].

The EW experiments were conducted in parallel plate configuration [24]. The explosive used was a 96:4 mixture of microporous ammonium nitrate and diesel oil ($d = 780 \text{ kg/m}^3$). Table 1 lists the EW modes. Explosive welding parameters (r , V_0 , and γ) were calculated using the equations presented in [25] (Table 1).

Fig. 1 Initial microstructure of the AlMg6

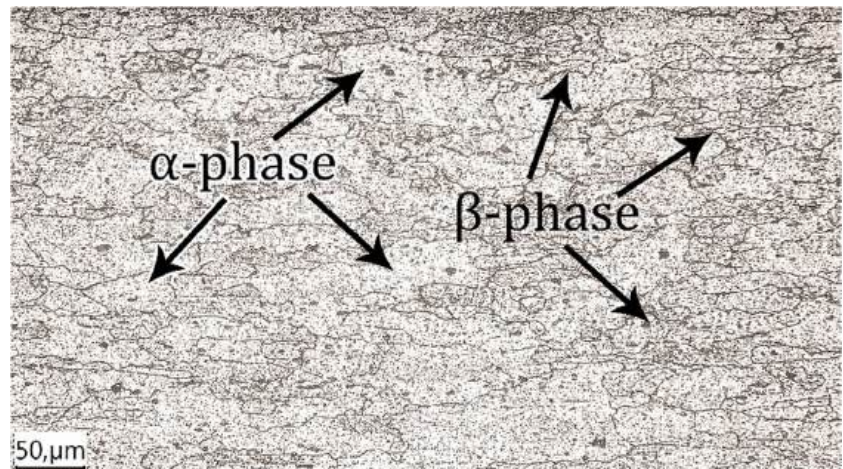


Table 1 EW parameters

Mode	Explosive ratio, r	Detonation velocity D , m/s	Flyer plate velocity V_0 , m/s	Collision angle γ , °
1	1.5	2000	600	17.2
2	2.6	2700	1100	23.6
3	3.7	3200	1535	27.8

2.2 Microstructural study

The specimens used for metallographic studies and mechanical tests were cut from bimetallic sheets using a DK7725 wire cut electrical discharge machine according to the scheme shown in Fig. 2.

The metallographic specimens were embedded in a BAKELIT GF conductive compound with a graphite filler using a METAPRESS-P metallographic press. Grinding and polishing were performed using a DIGIPREP machine. Grinding was carried out using emery papers with grit sizes of 320, 800, 1500 and 2500. Polishing was carried out using two water-based suspensions. One suspension contained 3- μm diamond particles, whereas the other contained 1- μm diamond particles. Superfinishing was carried out in an acid suspension of colloidal silicon oxide with a particle size of 0.05 μm . The identification of microstructural elements was performed by successive etching with Keller's reagent for 5–15 s and then with Vek's reagent for 60 s.

The metallographic studies were performed with a Carl Zeiss Axio Observer Z1m inverted metallographic microscope using the Thixomet PRO software package. SEM/EDS analysis was carried out with a Zeiss UltraPlus microscope equipped with an INCA 350 Oxford accessory.

To obtain further insight into the microstructure formed at the weld interface, electron backscatter diffraction (EBSD) was

applied. For this analysis, the final surface finish was obtained using conventional polishing techniques followed by long-term (24-h) vibratory polishing with a colloidal silica suspension. The EBSD observations were performed using an FEI Quanta 600 field emission gun scanning electron microscope equipped with TSL OIMTM EBSD software at an accelerating voltage of 20 kV. To investigate the microstructure at different length scales, three EBSD maps were obtained with scan step sizes of 0.5 μm , 0.2 μm , and 0.05 μm . To enhance the fidelity of the EBSD data, the fine grains comprising one or two pixels were eliminated from the EBSD maps using the standard grain-dilation option of the EBSD software. Owing to the limited angular accuracy of EBSD, poorly developed boundaries with misorientations below 2° were excluded from consideration. A 15° threshold was applied to differentiate low-angle boundaries (LABs) from high-angle boundaries (HABs).

A confocal laser scanning microscope (Optelics Hybrid LaserTec, Japan) was used to obtain confocal images and 3D visualizations of the surface of the weld interface after etching. The heat treatment (HT) of the specimens was conducted in a SNOL 8,2/1100 muffle furnace.

2.3 Mechanical and ultrasonic testing

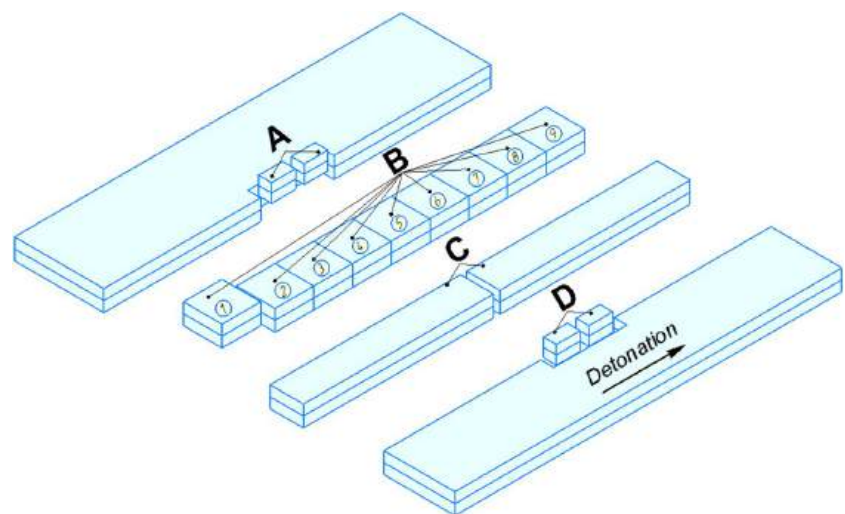
The microhardness (HV) was measured using a PMT-3 Vickers hardness tester and MMS software. Loads of 50 g were applied for 10 s.

Tear testing of the weld joint after EW was conducted on an Instron 1195 universal testing machine, as shown in Fig. 3.

The tear strength σ_t was subsequently calculated from the following equation:

$$\sigma_t = \frac{4P}{\pi(d_2^2 - d_1^2)}, \quad (1)$$

Fig. 2 Specimens for metallographic studies. **A, D** Specimens for metallographic study. **B** Specimens for tear strength test. **C** Bending test specimens



where P is the applied load, N ; d_1 is the inner diameter, mm; and d_2 is the outer diameter, mm.

Figure 4 shows the specimens used for tear strength testing.

To analyze the delamination resistance of the bending interface and ductility of the welded layers, the bending ductility of the AlMg6-AlMg6 composite plate was studied. The bending ductility test determines the angle of bend at which fracture occurs. The specimens used for the bending ductility test had dimensions of 8 mm (height), 20 mm (width), and 145 mm (length) and were cut from the central part of the bimetal along the plane parallel to the detonation direction (Fig. 5).

The scheme of the three-point bending test is shown in Fig. 6. The tests were carried out on the specimens before and after heat treatment. The heat treatment was applied at a temperature of 200 °C for 60 min with cooling in the furnace to room temperature. This heat treatment increases the ductility of the AlMg6-AlMg6 bimetal without reducing the weld interface strength [18].

Ultrasonic testing was performed using a UD2V-P45 apparatus with two separately combined converters with a test frequency of 5 MHz to detect delamination at the weld interface.

Table 2 shows all the symbols used in the research.

Fig. 3 Schematic diagram of tear testing. Tear specimen (a) Tear testing diagram (b): 1, mold; 2, base layer; 3, flyer layer; 4, male die

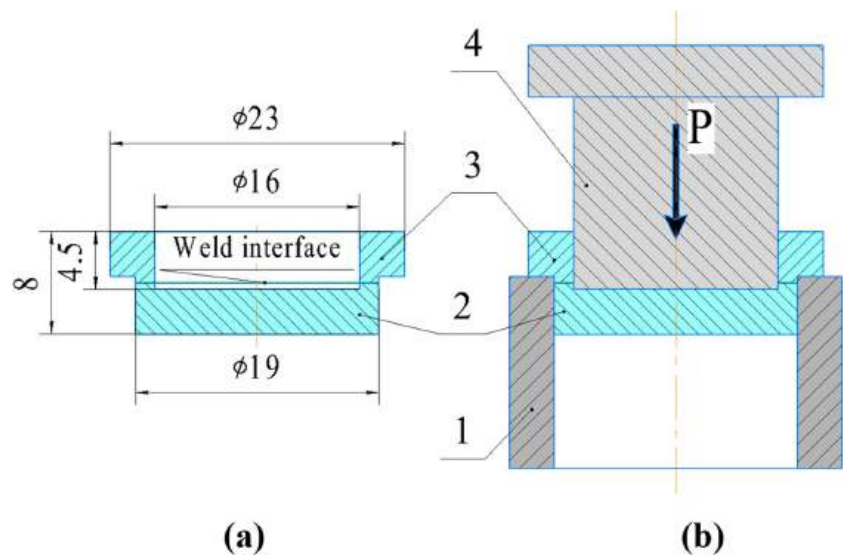
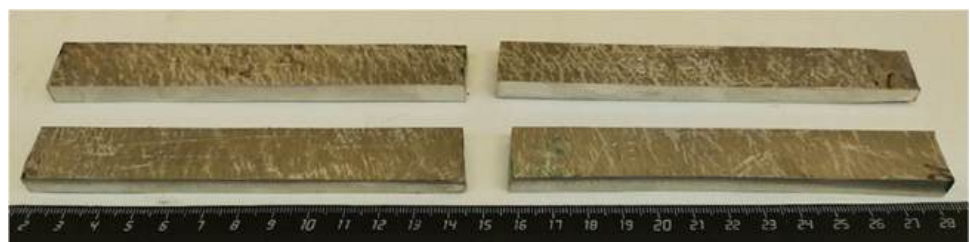


Fig. 4 Photograph of the tear test specimens

Fig. 5 Photograph of the bending test specimens



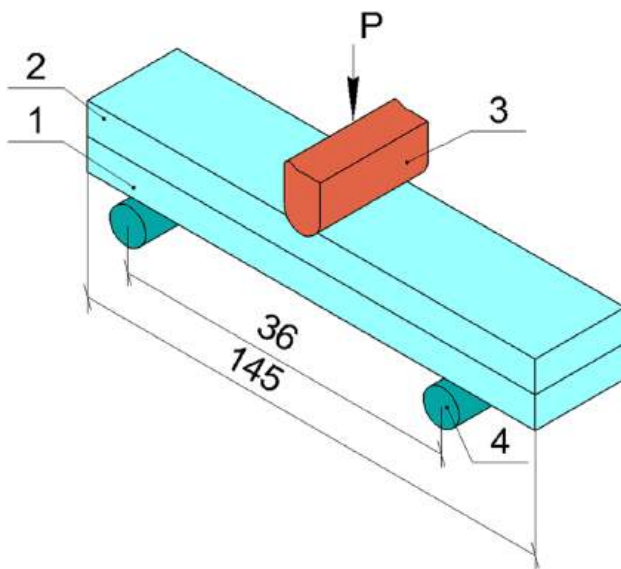


Fig. 6 Bending test: 1, base plate; 2, flyer plate; 3, mandrel; 4, specimen supports

Table 2 Nomenclature table with SI units

Symbol	Unit	Meaning
r	-	Explosive ratio
D	m/s	Detonation velocity
V_0	m/s	Flyer plate velocity
σ_t	MPa	Tear strength
P	N	The applied load
d_1	mm	Inner diameter of the specimen
d_2	mm	Outer diameter the specimen

3 Results and discussion

3.1 Ultrasonic testing results

The mode 1 parameters did not produce a joint due to the insufficient plastic deformation of the surfaces and the insufficient pressure of the detonation products on the surface of the flyer plate. Figure 7a and b show the specimens after EW according to modes 2 and 3 and ultrasonic testing. The delamination regions are located along the edges of the bimetallic specimens. The ultrasonic testing results revealed that the unflawed regions were approximately 80% of the total area of the bimetallic specimens. The delamination regions are caused by the partial dispersion of explosive particles in the environment.

3.2 Metallographic analysis results

Figure 8 shows the microstructure of the weld interface in specimens 2 (Fig. 8a) and 3 (Fig. 8c) after etching. The weld interface of specimen 2 is nearly straight (Fig. 8b), and the weld interface of specimen 3 is in the shape of a wave (Fig. 8d).

Extended dark dislocation structures are observed at the weld interface. These structures were detected due to their increased etchability. Additionally, the weld interface revealed an accumulation zone of a finely dispersed dark etched phase, presumably Mg_2Al_3 , with thicknesses of 4 μm in specimen 2 and 9 μm in specimen 3. Note that in specimen 2, this phase forms an almost continuous layer, whereas in specimen 3, it is fragmented into particles. In addition, in both specimens in the transition zone (i.e., the zone of structural changes), there are more pronounced adiabatic shear bands in specimen 3, which originate at the weld interface and extend into the flyer and base plates at an angle of 30° . The number, density, and enclosed volume increase in specimen 3 due to the higher collision velocity.

3.3 EBSD analysis

A series of EBSD maps of the material in the vicinity of the weld interface produced by mode 3 are shown in Figs. 9 and 10. To obtain comprehensive insight into the evolved microstructure, EBSD data were arranged as orientation maps (Fig. 9)¹ and grain-boundary maps (Fig. 10).

As expected, EW caused a sharp microstructural gradient at the weld interface. Specifically, three structural constituents can be defined: (I) a broad deformation zone, which extends $\sim 500 \mu m$ from the weld interface; (II) adiabatic shear bands; and (III) the weld interface.

In the deformation zone, essential grain compression was revealed (Fig. 9a), with this effect being most pronounced in close proximity to the weld interface (Fig. 9b). Moreover, the heavily compressed grains typically exhibited crystallographic orientations close to $\langle 110 \rangle // ND$ (where ND is the normal direction to the weld interface), thereby resembling a typical compression texture in face-centered cubic metals. This observation suggested that the strain mode during EW was likely close to axial compression.

The ASBs presented an increased concentration of deformation-induced boundaries as well as a more pronounced transformation of LABs into HABs (Fig. 9a). The

¹ Notably, EBSD data collected directly from the weld interface were of relatively low quality (presumably due to the high residual stress in this area). To avoid confusion, the pixels with a confidence index below 0.1 were excluded from consideration (and thus appeared black in Fig. 8c).

Fig. 7 Ultrasonic testing results: **a** delamination regions in specimen 2 and **b** in specimen 3

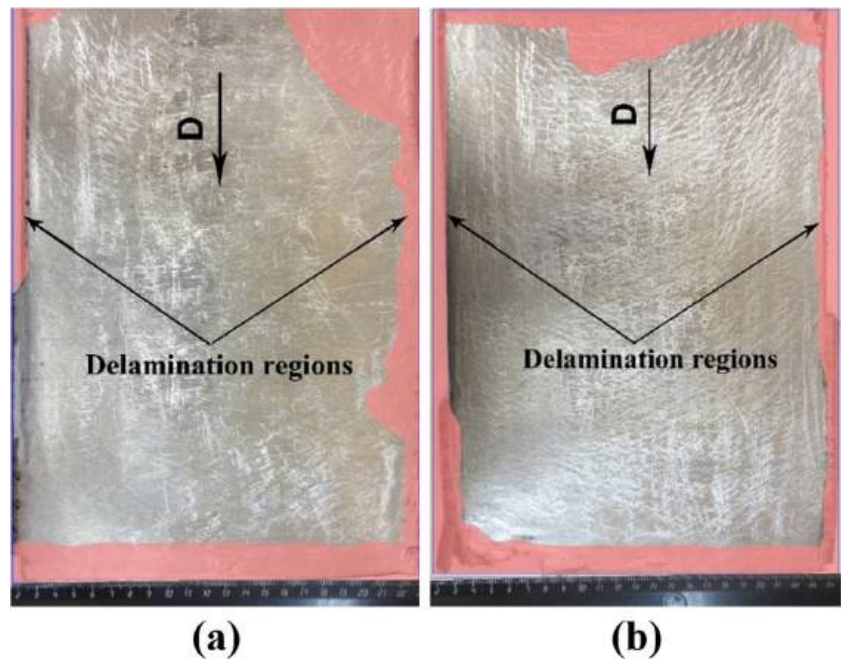
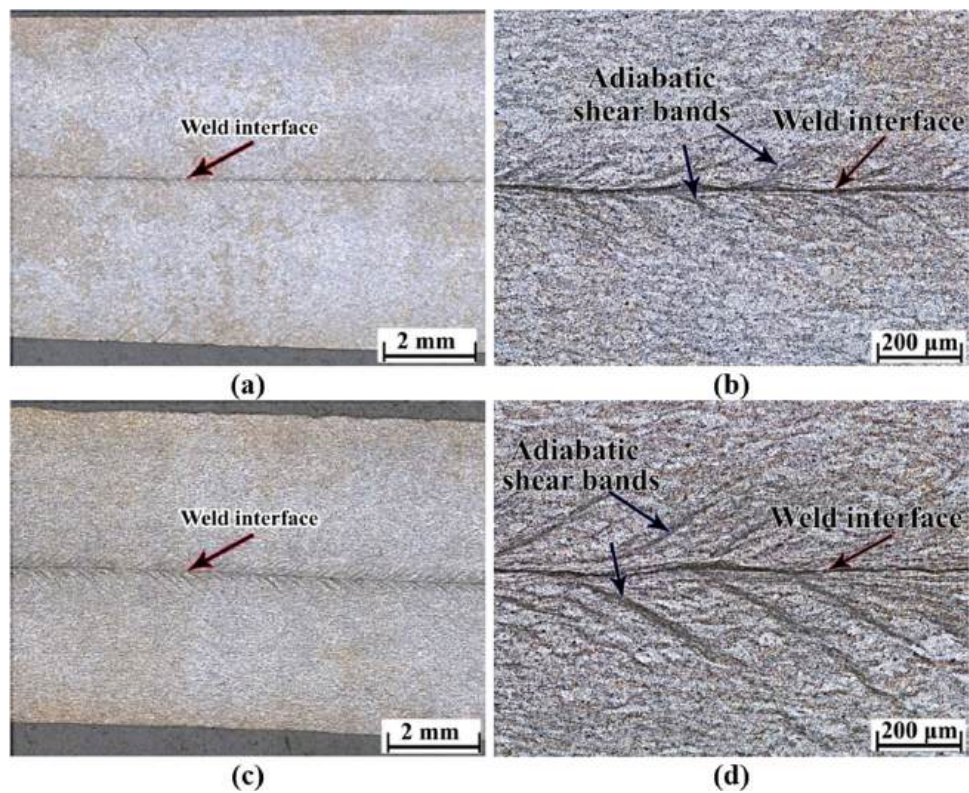


Fig. 8 Microstructure of the weld interface: specimen 2 (**a, b**) and specimen 3 (**c, d**)



microstructure of the weld interface was dominated by fine ($< 1 \mu\text{m}$), low-aspect grains, which presumably contained a high dislocation density (Fig. 9c). In some locations, surviving fragments of heavily compressed grains were observed (the selected area in Fig. 9c is outlined with a white line).

Remarkably, the width of such remnants was comparable to the characteristic size of the matrix fine-grained structure. Hence, it was likely that the microstructural evolution in this area was governed by the transverse subdivision of the compressed grains.

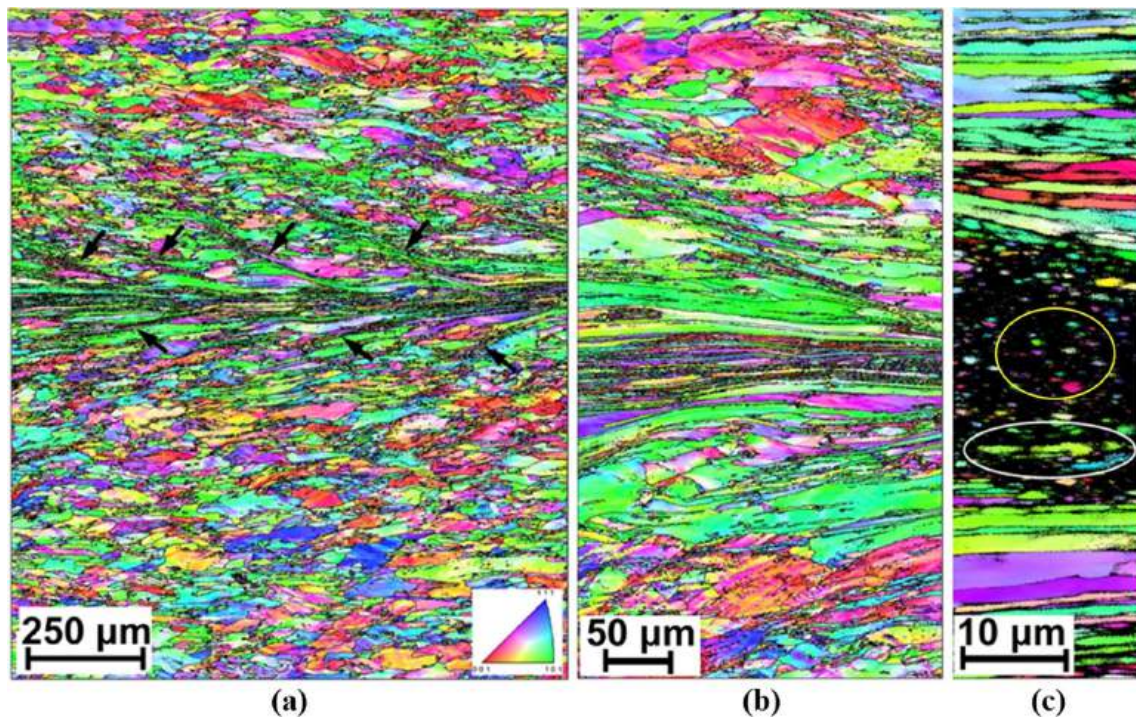
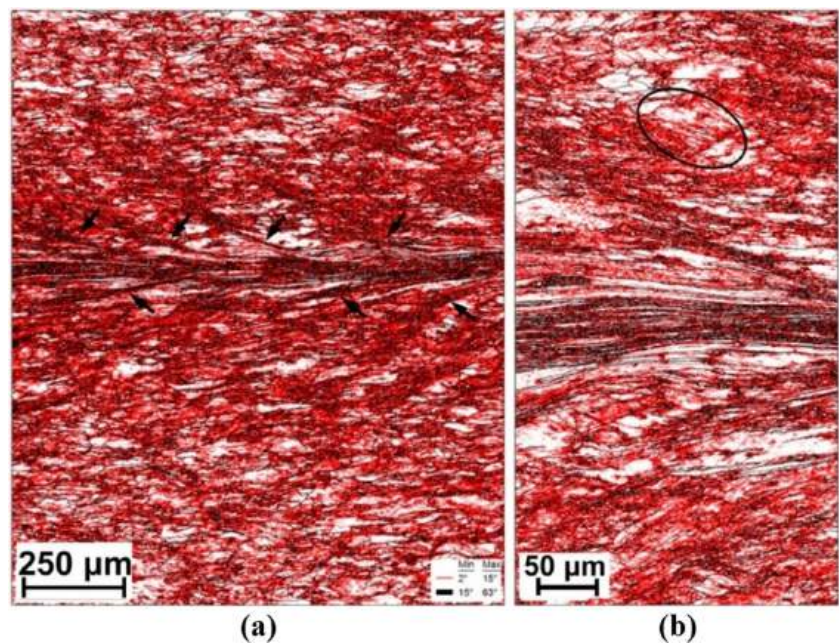


Fig. 9 EBSD orientation maps showing the microstructure evolution near the weld interface at different length scales: **a** low-magnification image, **b** high-magnification image, and **c** high-resolution map taken from the welded area. The individual pixels in the maps are colored according to their crystallographic orientation relative to the joint

surface normal (the color code triangle is shown in the bottom right corner of **a**, and HABs are depicted as black lines (LABs are omitted for simplicity). In **a**, arrows exemplify ASBs. In **c**, black pixels reflect the EBSD data with a low confidence index

Fig. 10 EBSD grain-boundary maps showing microstructure evolution near the weld interface at different length scales: **a** low-magnification image and **b** high-magnification image. LABs and HABs are depicted as red and black lines, respectively (the color code is shown in the bottom right corner of **a**). The arrows in **a** represent the ASBs. In **b**, the selected area exemplifies the grain subdivision process



Although the EW is extremely rapid process, recrystallization of deformed grains occurs. As a result, new grains formed at the weld interface (the selected area in Fig. 9c is

outlined with a yellow line). Similar results were obtained in [26] when the magnesium alloy AZ31B was welded with the aluminum alloy AA6061.

Moreover, extensive formation of deformation-induced boundaries was also found (Fig. 10a and b). In some cases, these grains were arranged in a distinct series that extended across almost the entire grain size (selected area in Fig. 10b). Some segments of such deformation boundaries exhibited misorientation above 15° , thus reflecting the activation of the grain-subdivision mechanism. However, such observations are rare, and deformation-induced boundaries are typically poorly developed. No massive LAB-to-HAB transformation was revealed. This result is likely associated with the relatively short duration of the deformation process during EW. This should retard diffusion-assisted processes and thus slow the evolution of deformation-induced boundaries.

3.4 Confocal laser scanning microscopy and EDS line scan analysis

Figure 11a shows a confocal image of the weld interface in specimen 3. Due to the formation of high values of first- and second-order stresses at the weld interface after EW, stress corrosion occurs as a result of etching, which leads to deeper corrosion at the weld interface (up to $0.5 \mu\text{m}$) than at the layers of the bimetal (Fig. 11b).

Fig. 11 Confocal image of the weld interface surface after etching: **a** weld interface with transverse line profile; **b** height profile of the weld interface surface

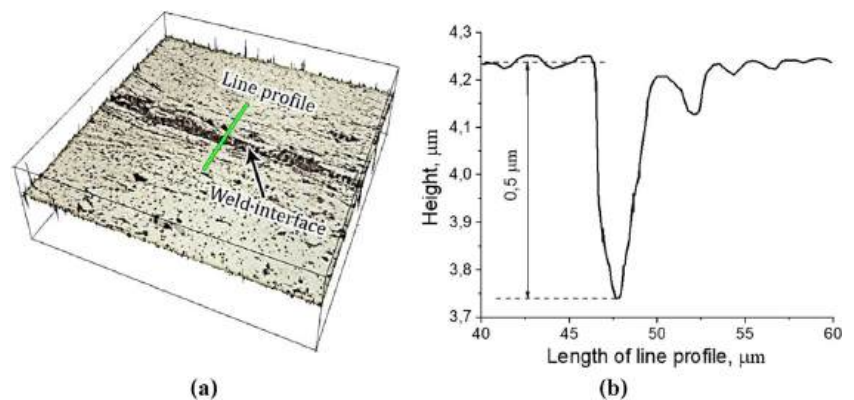
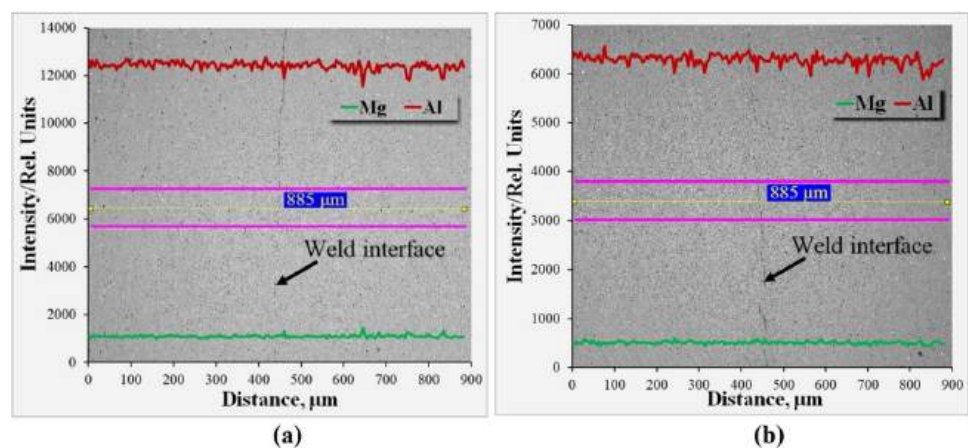


Fig. 12 EDS line scans of the Al and Mg concentrations across the weld interface: specimen 2 (**a**) and 3 (**b**)



EDS line scan analysis revealed that Al and Mg were uniformly distributed near the weld interface (Fig. 12a and b). Thus, modes 2 and 3 provide homogeneous chemical compositions of the welded plates at the macroscopic level. Moreover, there are both peaks and dips on the lines of Al and Mg, which indicates the nonuniformity of the concentration of these elements in the AlMg6 alloy at the microscopic level.

3.5 Effects of heat treatment

AlMg6 is a non-heat-treatable aluminum alloy. The strengthening of these alloys is achieved by work hardening. Figure 11 shows the microstructure of the weld interface after HT. Specimens 2 (Fig. 13a) and 3 (Fig. 13c) did not show any microstructural changes after HT at 200°C . However, HT at 550°C removed the work hardening zone and formed a recrystallized structure near the weld interface, where the grains of the flyer plate merged with the grains of the base plate, as shown by the red arrow in Fig. 11b. The HTs also formed a recrystallized structure in the ASBs. The shape of the recrystallized grains is predominantly uniaxial (Fig. 13b and d). The width of the recrystallization zone in both specimens is approximately $500 \mu\text{m}$.

Fig. 13 Microstructure of the weld interface after HT: specimen 2 (a 200 °C, b 550 °C); specimen 3 (c 200 °C, d 550 °C)

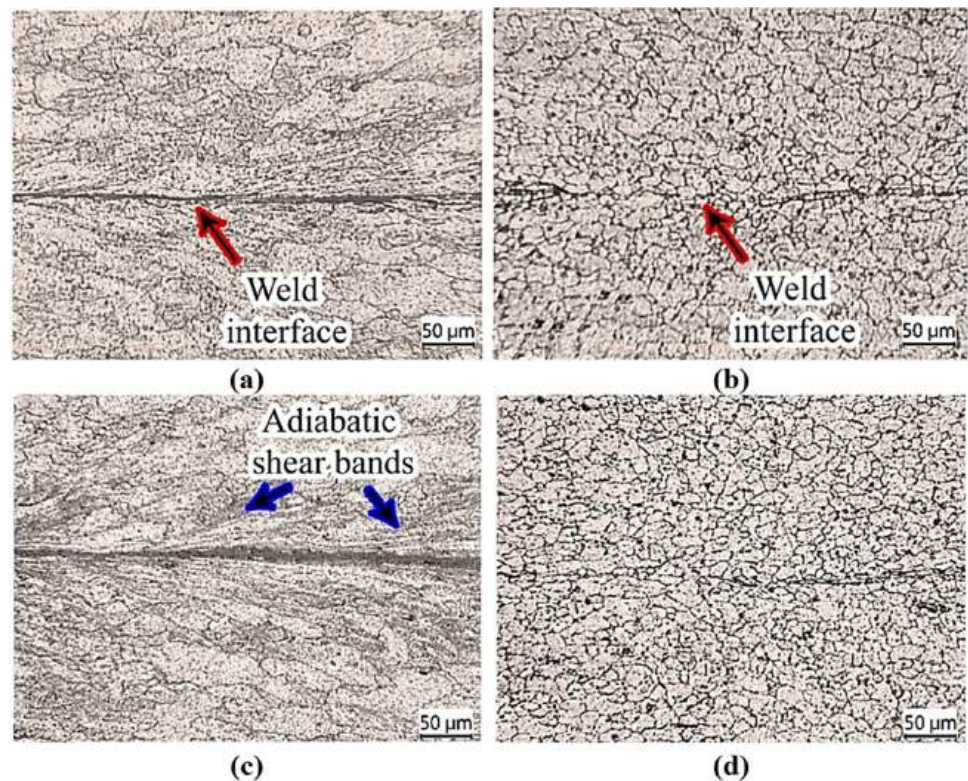


Figure 14 shows the microhardness distribution along the thickness of the specimens. The dashed lines show the microhardness of the initial plate of AlMg6 before and after HT at 200 °C. HT partially removed the work hardening in the initial plates that were manufactured by rolling and thus decreased the microhardness by approximately 18%.

The blue points indicate the microhardness of the AlMg6-AlMg6 bimetal after EW. Both specimens exhibit a sharp decrease in the microhardness at the weld interface. This decrease suggested that dynamic recrystallization of the grains and aging of the AlMg6 occurred due to extreme heating followed by rapid cooling of the weld interface. The sources of heat are shock-compressed gas in the gap [27] and severe plastic deformation of the surfaces during collision. Recrystallization reduces the dislocation density. This reduces the strength of the material while increasing the ductility [28].

It is well known that after EW, a work hardening zone [29–31] is formed in the material from the weld interface deep into the plates. This zone can have different widths, depending on the material properties and the EW parameters. In this study, after EW, the microhardness near the weld interface was approximately 220 HV, which was 20% greater than that of the initial plate. This higher microhardness is due to the work hardening in the base and flayer plates. The width of the work-hardened zone is approximately 1 mm in specimen 2 and 2 mm in specimen 3. The microhardness in this zone after HT at 200 °C is 160 HV, which is close

to that of the initial plate. The microhardness in this zone after HT at 550 °C is 110 HV for specimen 2 and 120 HV for specimen 3. The lower microhardness is partly related to dislocations disappearing and grains recrystallizing [32].

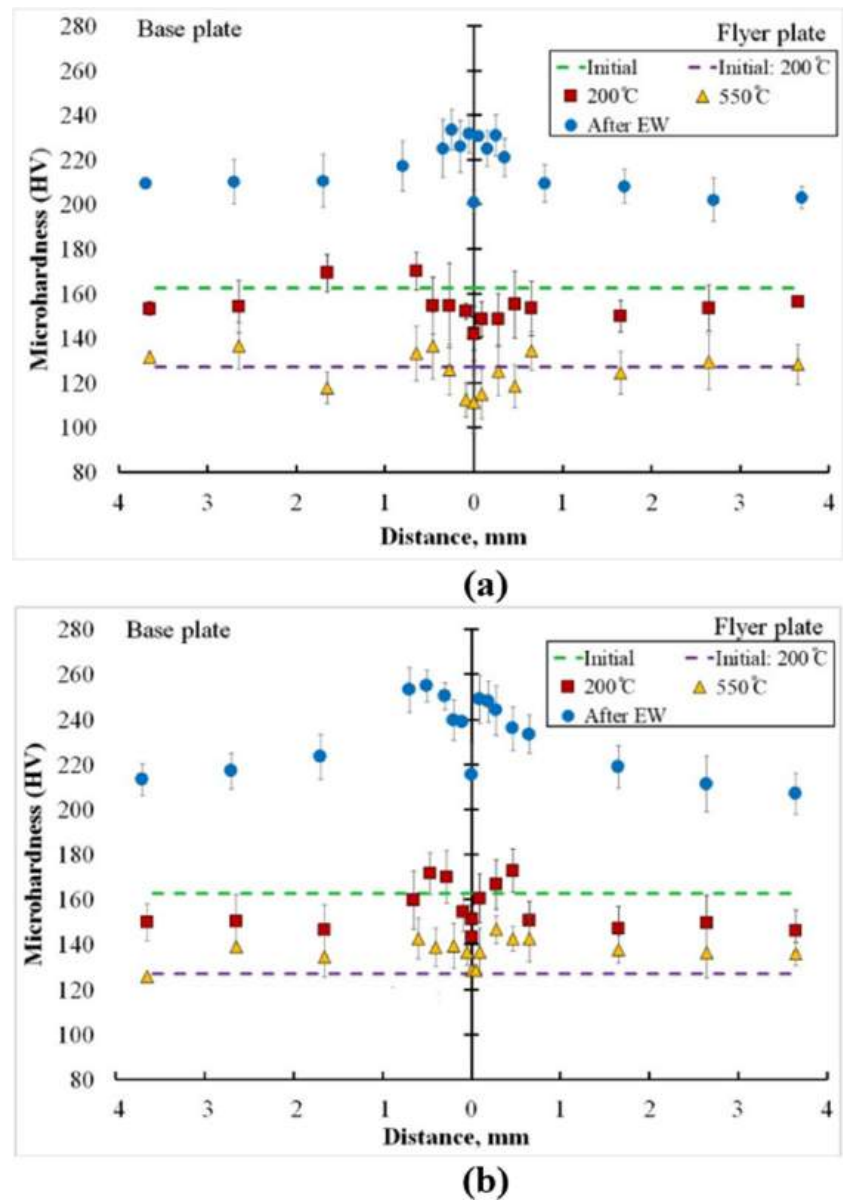
3.6 Mechanical test results

The average tear strength in specimen 2 is 80 ± 10 MPa, and that in specimen 3 is 230 ± 10 MPa. Mechanical testing of specimen 3 revealed three distinct zones of tear strength. The first zone (from 0 to 100 mm) has a low strength (≤ 76 MPa). This is because it takes some time for the pressure to reach the necessary values to form a strong joint. The second zone (from 100 to 180 mm) shows a uniform tear strength distribution (113–128 MPa). The third zone (from 200 to 290 mm) has the highest tear strength (204–242 MPa), and the average tear strength in this zone is 228 MPa, which is 35% lower than the ultimate tensile strength of the initial AlMg6 plate.

In [33], it was shown that most of the residual stresses after EW accumulate near the weld interface and decrease the ductility of the bimetal. The effects of residual stresses, the work hardening zone, and LSBs on the ductility of the AlMg6-AlMg6 bimetal were investigated via a bending test (Fig. 15).

The untreated specimens without heat treatment survive at a smaller bend angle. Figure 15a shows that at a bend angle of 64° , a crack developed in the outer layer of the

Fig. 14 Microhardness distributions in specimen 2 (a) and specimen 3 (b)



bimetal (specimen 2), extending to the weld interface and contributing to delamination at the point of maximum tensile stress. This crack was formed as a result of a combination of the following factors: the work hardening zone formed throughout the thickness of the bimetal, the presence of localized shear bands, and residual stresses at the weld interface. Since the inner layer is compressed and the outer layer is stretched, the crack is located in the outer layer. Figure 15c shows specimen 3 subjected to a 57° bend angle. The crack also started in the outer layer and propagated to the weld interface, and no delamination was observed.

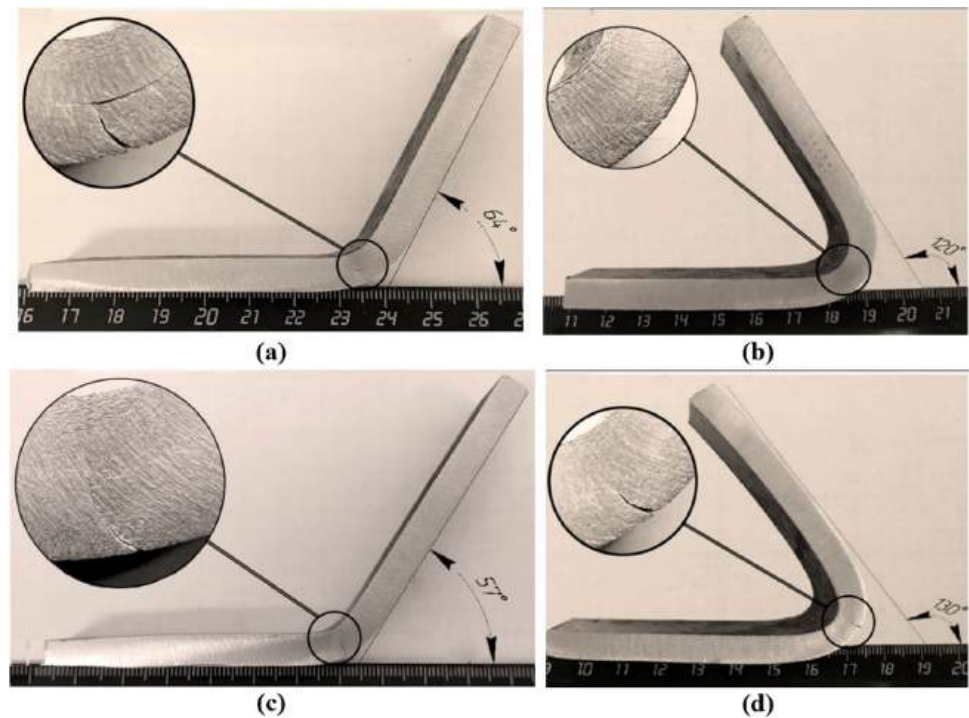
Figure 15b and d show heat-treated specimens 2 and 3 after the bending test. These specimens survive at twice the bending angle. At the same time, the cracks had a shorter propagation length, and there was no delamination at the

weld interface. Thus, the heat treatment mode used is generally suitable for partial stress relief and adiabatic shear bands without a noticeable reduction in strength. For example, heat treatment at 200°C doubled the ductility of AMg6 after EW, removing internal stresses and work hardening to the original material level (Fig. 14).

4 Conclusions

This study determined the conditions for obtaining a strong joint of AlMg6 with AlMg6, as well as the influence of heat treatment on the weld interface and the properties of the bimetal. From the point of view of strength and plastic properties, the use of mode 3 (specimen 3) is promising.

Fig. 15 Bending test results: **a** bend specimen (EW mode 2), **b** bend specimen (EW mode 2, heat-treated), **c** bend specimen (EW mode 3), **d** bend specimen (EW mode 3, heat-treated)



In this case, it is necessary to minimize the effect of the shock-compress gas (SCG) in the welding gap on the weld interface. To minimize the effect of SCG, inert gases (Ar, He) can be injected into the gap or create a vacuum between the plates. One work [34] reported that when welding in a vacuum, the pressure in the SCG decreases several times, and accordingly, the temperature of the SCG also decreases. In this way, the joint is formed under deformation conditions of the surface grains of AlMg6. The conclusions of this research can be summarized as follows:

- EBSD analysis revealed that the EWs produced three distinctive microstructural zones in the AlMg6: a zone of deformed grains (crystallographic orientations close to $\langle 110 \rangle$), a zone of ASBs, and the weld interface.
- Substantial compression and elongation of the grains occurred in the zone of the deformed grains (size of $< 1 \mu\text{m}$), which led to the formation of deformation boundaries at large misorientation angles. These deformation boundaries are also observed in the zone of ASBs as well as during the transformation of LABs into HABS. The weld interface shows the presence of fine grains, which indicates that fragmentation of the deformed grains may have occurred during the EW process. Therefore, the formation of a joint during the EW of AlMg6 with different materials is possible only under the condition of maximum grain compression deformation on the surface to be joined.
- The study of the effect of HT on the microstructure of the AlMg6-AlMg6 bimetal showed that HT at 200°C for 1 h did not remove ASBs from either layer of AlMg6. Additionally, heating relieves residual stresses and work hardening, which occur at the weld interface, and the mechanical properties become close to those of the initial material.
- A heat treatment at 550°C partially removed the weld interface, which indicates that recrystallization of the grains occurred. The width of the recrystallization zone in both specimens is approximately $500 \mu\text{m}$. Thus, at the interface between the homogeneous materials obtained by explosive welding, stresses are created that accelerate the diffusion processes when heated above $0.8T_{\text{m.p.}}$, reducing the recrystallization time, the disappearance of the interface between the welded plates, and the formation of a homogeneous material structure and properties.
- The study of microhardness revealed that its change with increasing distance from the weld interface in all specimens has the same characteristics. The maximum value is found in the areas $300\text{--}400 \mu\text{m}$ from the weld interface. The weld interface has a low microhardness, which is due to the presence of pores after etching, as detected by confocal laser scanning microscopy.
- Tear testing of the weld joint has shown that higher EW parameters lead to a much greater tear strength (from 80 to 230 MPa) with a nonuniform distribution along the plate, which is attributed to the nonuniform impact of gaseous detonation products and the thermodynamic parameters of the shock-compressed gas.
- The results of the bending test revealed that after explosive welding, the specimens were in a stress–strain state, which reduced the ductility of the bimetal (the bend angle was approximately 60°). However, after heat treatment at 200°C

for 1 h, the specimens survived at twice the bending angle (approximately 130°), indicating good plastic properties.

- In future experiments, we plan to conduct experiments using inert gases in the welding gap and in a vacuum environment. These experiments help us understand how the gas composition affects the microstructure at the weld interface and, as a result, the mechanical properties.

Acknowledgements The authors are grateful to Dr. Mikhail Zhidkov for his interest in their work and for assistance with confocal laser scanning microscopy. This research was funded in accordance with the state task of Merzhanov Institute of Structural Macrokinetics and Materials Science of the Russian Academy of Sciences (ISMAN) No. 122-032-800-153-5. This research was performed using the set of modern scientific instruments available for multiple access at the ISMAN Center of Shared Services. This research was performed using a set of modern scientific instruments available for multiple access at the Polzunov Altai State Technical University Center of Shared Services. This work was performed under the framework of the Development Program of Belgorod National Research University for 2021-2030 (“Priority 2030”). EBSD measurements were performed using the equipment of the Joint Research Center “Technology and Materials” at Belgorod National Research University (financial support from the Ministry of Science and Higher Education of the Russian Federation under agreement No. 075-15-2021-690, the unique project identifier RF 2296.61321X0030).

Author contribution Andrey Malakhov: conceptualization, methodology, formal analysis, visualization, writing—review. Ivan Saikov: supervision, data curation and editing. Igor Denisov: investigation, writing—review and editing. Alexander Berdyachenko: writing—original draft and methodology. Sergey Ivanov: formal analysis, software, and investigation. Nemat Niyozbekov: writing—original draft and investigation. Sergey Mironov: formal analysis, software, and writing—original draft. Rustam Kaibyshev: methodology, software, and formal analysis. Pavel Dolzhenko: formal analysis, validation, and methodology.

Funding This research was funded in accordance with the state task of Merzhanov Institute of Structural Macrokinetics and Materials Science of Russian Academy of Sciences (ISMAN) No. 122-032-800-153-5, Polzunov Altai State Technical University Center of Shared Services and Belgorod National Research University (financial support from the Ministry of Science and Higher Education of the Russian Federation under the agreement No. 075-15-2021-690, the unique project identifier RF 2296.61321X0030).

Declarations

Consent to participate All the authors participated in this research.

Conflict of interest The authors declare no competing interests.

References

- Vasu K, Chelladurai H, Addanki R, Malarvizhi S, Balasubramanian V (2009) Effect of fusion welding processes on tensile properties of armor grade, high thickness, nonheat treatable aluminum alloy joints. *Defence Technol* 15:353–362. <https://doi.org/10.1016/j.dt.2018.11.004>
- Xiang C, Daisuke I, Shigeru T, Akihisa M, Xiaojie Li, Kazuyuki H (2020) Explosive welding of Al alloys and high strength duplex stainless steel by controlling energetic conditions. *J Manuf Process* 58:1318–1333. <https://doi.org/10.1016/j.jmapro.2020.09.037>
- Wang S, Xu L, Sun T, Li G, Cui J (2021) Effects of process parameters on mechanical performance and interfacial morphology of electromagnetic pulse welded joints between aluminum and galvanized steel. *J Mater Res Technol* 10:552–564. <https://doi.org/10.1016/j.jmapro.2020.09.037>
- Mazar Atabaki M, Nikodinovski M, Chenier P, Ma J, Harooni M, Kovacevic R (2014) Welding of aluminum alloys to steels: an overview. *J Manuf Sci Prod* 14:59–78. <https://doi.org/10.1515/jmsp-2014-0007>
- Junaid M, Cheema TA, Haleem H, Saad-ul-Fatah RK, Park CW (2018) Effects of thermal material properties on precision of transient temperatures in pulsed laser welding of Ti6Al4V alloy. *Proc Inst Mech Engineers, Part C: J Mech Eng Sci* 233:3170. <https://doi.org/10.1177/0954406218802604>
- Daha MA, Nassef GA, Abdallah IA (2012) Numerical modeling of heat transfer and fluid flow in keyhole plasma arc welding of dissimilar steel joints. *Int J Engi Sci and Tech* 4:506
- Dong H, Hu W, Duan Y, Wang X, Dong C (2012) Dissimilar metal joining of aluminum alloy to galvanized steel with al-si, al-cu, al-si-cu and zn-al filler wires. *J Mater Process Technol* 212:458–464. <https://doi.org/10.1016/j.jmatprotec.2011.10.009>
- Ahmed MMZ, Jouini N, Alzahrani B, Seleman MME-S, Jhaheen M (2021) Dissimilar friction stir welding of AA2024 and AISI 1018: microstructure and mechanical properties. *Metals* 11:330. <https://doi.org/10.3390/met11020330>
- Hong S, Ran Q, Yi T, Hua Y, Yin D (2011) Study on the joining characteristics of diffusion welding lap joint with various temperatures between aluminum alloy and stainless steel. *Adv Mat Res* 291–294:1003–1006. <https://doi.org/10.4028/www.scientific.net/AMR.291-294.1003>
- Haddadi F, Prangnell P (2013) Grain structure evolution in aluminum to steel ultrasonic spot welding. *Mater Sci Technol Conf Exhib* 2:1252–1259. <https://doi.org/10.13140/2.1.4317.1209>
- Cui GM, Li XX, Zeng JM (2012) Research on cold-rolled bimetal of high-tin aluminum alloy and steel. *Appl Mech Mater* 217–219:395–399. <https://doi.org/10.4028/www.scientific.net/amm.217-219.395>
- Yu H, Tong Y (2017) Magnetic pulse welding of aluminum to steel using uniform pressure electromagnetic actuator. *Int J Adv Manuf Technol* 91:2257–2265. <https://doi.org/10.1007/s00170-016-9928-y>
- Makhina DN, Nikulin SA, Denisov VN, Klyatskin AS (2020) Effect of the production conditions on the structure and strength of the AMg6 Alloy–12Kh18N10T steel bimetallic joint. *Russian Metallurgy (Metally)* 10:1095–1101. <https://doi.org/10.1134/S003602952010016X>
- Palaci Y, Olgun M (2021) Influences of heat treatment on mechanical behavior and microstructure of the explosively welded d grade steel/EN AW 5083 aluminum joint. *Arch Metall Mater* 66:373–380. <https://doi.org/10.24425/amm.2021.135868>
- Carvalho GHSFL, Galvão I, Mendes R, Leal RM, Loureiro A (2020) Explosive welding of aluminum to stainless steel using carbon steel and niobium interlayers. *J Mater Process Technol* 283:116707. <https://doi.org/10.1016/j.jmatprotec.2020.116707>
- Wang JM, Zhang Y (2013) A study on weldability of aluminum alloy-aluminum-steel transition joints. *Adv Mat Res* 631–632:713–716. <https://doi.org/10.4028/www.scientific.net/amr.631-632.713>
- Zhang T, Wang W, Yan Z, Zhang J (2021) Interfacial morphology and bonding mechanism of explosive weld joints. *Chin J Mech Eng* 34:8. <https://doi.org/10.1186/s10033-020-00495-7>

18. Malakhov A, Denisov I, Niyozbekov N, Saikov I, Shakhray D, Sosikov V, Emelyanov A (2024) Theoretical and experimental studies of the shock-compressed gas parameters in the weld gap. *Materials* 17:265. <https://doi.org/10.3390/ma17010265>
19. Kumar P, Ghosh SK, Barma SS, JD, (2023) Experimental and simulation studies on explosive welding of AZ31B-Al 5052 alloys. *Int J Adv Manuf Technol* 127:2387–2399. <https://doi.org/10.1007/s00170-023-11684-8>
20. Sedighi M, Honarpisheh M (2012) Experimental study of through-depth residual stress in explosive welded Al–Cu–Al multilayer. *Mater Des* 37:577–581. <https://doi.org/10.1016/j.matdes.2011.10.022>
21. Rittel D, Peri L, Venkert A (2008) Dynamic recrystallization as a potential cause for adiabatic shear failure. *Phys Rev Lett* 101:165501. <https://doi.org/10.1103/PhysRevLett.101.165501>
22. Malakhov AY, Saikov IV, Denisov IV, Berdychenko AA, Ivanov SG, Niyozbekov NN (2023) AlMg6–AlMg6 weld interface: microstructure and mechanical properties after explosive welding. *J Adv Mater Technol* 8:304–315. <https://doi.org/10.17277/jamt.2023.04.pp.304-315>
23. Ren L, Gu H, Wang W, Wang S, Li C, Wang Z, Zhai Y, Ma P (2019) Effect of Mg content on microstructure and properties of Al–Mg alloy produced by the wire arc additive manufacturing method. *Materials* 12:4160. <https://doi.org/10.3390/ma12244160>
24. Malakhov AY, Saikov IV, Denisov IV, Niyozbekov NN (2020) AlMg6 to titanium and AlMg6 to stainless steel weld interface properties after explosive welding. *Metals* 10:1500. <https://doi.org/10.3390/met10111500>
25. Saikov IV, Malakhov AY, Saykova GR (2020) Influence of explosion welding parameters on the structure of the interfacial boundary in the thermobimetal brass-invar. *Inorg Mater Appl Res* 11:448–452. <https://doi.org/10.1134/S2075113320020331>
26. Mihara-Narita M, Asai K, Mori H, Saito N, Chino Y, Sato H, Watanabe Y (2023) Effects of annealing on the interfacial microstructure and mechanical properties of explosively welded AZ80 magnesium alloy and A6005C aluminium alloy. *Weld Int* 37:597–606. <https://doi.org/10.1080/09507116.2023.2228039>
27. Lee EH, Ko S (2018) A study on forming process of AA5083 alloy with an infrared local heat treatment. *IOP Conf Series: Mater Sci Eng* 418:012025. <https://doi.org/10.1088/1757-899X/418/1/012025>
28. Malakhov AY, Saikov IV, Denisov IV (2021) Brass/Invar bimetal by explosive welding. *Int J Adv Manuf Technol* 114:357–364. <https://doi.org/10.1007/s00170-021-06897-8>
29. He Y, Zhang S, Ding Q, Wang G, Liu F, Ma Y (2022) Comprehensive investigation of microstructural inhomogeneity in the bonding zone of explosive-welded AISI 410S/A283GrD composite. *Compos Interfaces* 29:57–77. <https://doi.org/10.1080/09276440.2021.1890426>
30. Li Y, Wu Z (2017) Microstructural characteristics and mechanical properties of 2205/AZ31B laminates fabricated by explosive welding. *Metals* 7:125. <https://doi.org/10.3390/met7040125>
31. Li CH, Li CM, Chen DM (2013) Influence of heat treatment on corrosive property of 5083 aluminum alloy. *Adv Mater Res* 779–780:205–211. <https://doi.org/10.4028/www.scientific.net/AMR.779-780.205>
32. Chu Q, Xia T, Zhao P, Zhang M, Zheng J, Yan F, Cheng P, Yan C, Liu C, Luo H (2022) Interfacial investigation of explosion-welded Al/steel plate: the microstructure, mechanical properties and residual stresses. *Mater Sci Eng* 33:142525. <https://doi.org/10.1016/j.msea.2021.142525>
33. Herdawandi H, David W, Marek N (2007) The Portevin-Le Chatelier (PLC) effect and shear band formation in an AA5754 alloy. *Acta Mater* 55:4151–4160. <https://doi.org/10.1016/j.actamat.2007.03.007>
34. Li X, Zhang T, Dai X et al (2024) Hazardous effects and microstructure of explosive welding under vacuum environment. *Int J Adv Manuf Technol* 130:3741–3754. <https://doi.org/10.1007/s00170-023-12892-y>

Publisher's Note Springer Nature remains neutral with regard to jurisdictional claims in published maps and institutional affiliations.

Springer Nature or its licensor (e.g. a society or other partner) holds exclusive rights to this article under a publishing agreement with the author(s) or other rightsholder(s); author self-archiving of the accepted manuscript version of this article is solely governed by the terms of such publishing agreement and applicable law.